Supporting Information

Hsieh et al. 10.1073/pnas.1718557115

SI Text

Starting Materials and Sample Preparation. Chemically homogeneous single crystals of (Mg,Fe)O Fp were synthesized by interdiffusion of Fe and Mg between a single-crystal MgO and presynthesized powder (Mg,Fe)O in an H_2/CO_2 gas-mixing furnace at the Institute for Planetary Materials, Okayama University at Misasa (13). Chemical compositions of the (Mg,Fe)O Fp were characterized by an electron probe and determined to be $Mg_{0.92}Fe_{0.08}O$ (Fp8), $Mg_{0.9}Fe_{0.1}O$ (Fp10), and $Mg_{0.44}Fe_{0.56}O$ (Fp56). Crystalline quality and lattice parameters of the synthesized samples were evaluated using X-ray diffraction at 13IDD beamline of the GSECARS of the Advanced Photon Source. Each of the Fp crystals (~50 × 50 μm^2) was polished down to a thickness of ~10 μm, coated with ~80-nm-thick Al film, and subsequently loaded together with a small ruby sphere into a symmetric diamond anvil cell (DAC) with a pair of anvil culets of 200 or 300 μm. Silicone oil (Chemical Abstracts Service no. 63148–62-9 from ACROS ORGANICS) was then loaded into the sample chamber as the pressure medium. The pressure in the chamber was determined by measuring ruby fluorescence spectra (48) before and after the thermal conductivity measurements, and the uncertainties of the pressure were typically <5%.

High-Pressure Lattice Thermal Conductivity Measurements. The lattice thermal conductivity of Fp was measured at high pressure and room temperature using time domain thermoreflectance (TDTR) coupled with a DAC. In our TDTR experiments, the output of a mode-locked Ti:sapphire oscillator laser was split into pump and probe beams. The pump beam heated the surface of Al film on the sample, creating temperature variations. The probe beam then detected the resulting changes in the optical reflectivity induced by the temperature changes on the Al film as a function of the time delayed between pump and probe beams. The in-phase V_{in} and out-of-phase V_{out} components of the variation of the reflected probe beam intensity, which were synchronized with the 8.7-MHz modulation frequency of the pump beam, were measured using an Si photodiode as well as a radio-frequency lock-in amplifier. The details of the TDTR are described elsewhere (49, 50).

The lattice thermal conductivity of the Fp in a high-pressure DAC was determined by comparing the time dependence of the ratio $-V_{in}/V_{out}$ to calculations based on a thermal model that takes into account heat flow into the sample substrate and into the pressure medium silicone oil (51, 52). Example data for Fp 10 at high pressures along with calculations by the heat flow model are shown in Fig. S2. The thermal model contains a number of parameters—laser spot size, thickness of Al film, thermal conductivity, and heat capacity of each layer—but the thermal conductivity of the Fp is the only significant unknown and free parameter to be determined. Under our experimental conditions, the ratio $-V_{in}/V_{out}$ during the delay time of a few hundred picoseconds is sensitive to and scales with the sum of the thermal effusivities of the Fp and silicone oil divided by the heat capacity per unit area of the Al film (details are in ref. 53). The thickness of Al film at ambient pressure was measured in situ by picosecond acoustics, and estimates of the changes in Al thickness at high pressures were described in ref. 54: Al thickness decreases by 10.3% at 25 GPa, by 12.6% at 40 GPa, by 15.2% at 70 GPa, and by 17.3% at 120 GPa. Since the thermal penetration depths in the Fp and silicone oil are of the order of hundreds of nanometers at the modulation frequency of the pump beam (8.7 MHz) (55), the thermal model is insensitive to their thicknesses (~10 μm) (Fig. S3 *A* and *B*). The thermal conductivity of the Al film at ambient pressure, ~200 W m^{-1} K^{-1} (53), is large and has essentially no effect on the thermal model calculations (Fig. S3*C*), and therefore, we fix this value at high pressures.

We estimated the pressure dependence of Al heat capacity using the atomic density and elastic constants of Al at high pressures along with calculations of Debye temperature as described in ref. 55. The thermal effusivity (square root of the product of thermal conductivity and volumetric heat capacity) of silicone oil at room temperature and up to 24 GPa was taken from ref. 56; for P = 24 to 120 GPa, the thermal effusivity was estimated by extrapolation based on the data below 24 GPa that were fitted into a polynomial, assuming that the silicone oil remains in an amorphous phase at high pressures. Compared with the Fp, the exceptionally low thermal effusivity of silicone oil at high pressures substantially reduces the uncertainty of the sample thermal conductivity, since it has only minor effects, typically less than 5% uncertainty, on the derivation of the thermal conductivity based on the thermal model (Fig. S3*D*).

The heat capacities of the Fp8, Fp10, and Fp56 at room temperature and high pressures are unknown. First principles calculations (57) showed that the heat capacity of Fp12.5 at high pressures is close to that of MgO. We, therefore, assume that the pressure dependence of the heat capacities of Fp8 and Fp10 is close to MgO taken from ref. 57. For Fp56, we assume that its heat capacity is close to Fp18.75 taken from ref. 58. We calculated the uncertainty in the thermal conductivity of Fp resulting from the uncertainty in each of the parameters used in our thermal model by evaluating the sensitivity of the thermal model to input parameters (cf. refs. 53 and 59 for details of the uncertainty evaluation) (example tests are shown in Fig. S3). It is important to note that precise determination of the thermal conductivity requires higher sensitivity to the thermal conductivity of Fp but lower sensitivity to other input parameters. We found that uncertainties in all of the parameters propagate to ~10% error in the measured thermal conductivity of Fp below 30 GPa, ~20% error at 60 GPa, and ~25% error at the highest pressure of 120 GPa.

Thermal Transport in Fp Across the Spin Transition of Iron. As shown in Fig. 1 and Fig. S1, the iron substitution in high-spin Fp reduces the lattice thermal conductivity as iron ions scatter phonons not only by the differences in mass and bonding strength between iron and magnesium ions (phonon-defect scattering) but also, by the resonant scattering effect of t_{2g} electronic energy levels of Fe^{2+} (Γ_{5g} state transitions to the nearly degenerate Γ_{4g} and Γ_{3g} states) that enables resonant scattering with thermal phonons (30) (resonant spin-phonon scattering). As pressure increases, the enhanced energy gap between Γ_{5g} and Γ_{4g}/Γ_{3g} states couples to higher-frequency thermal phonons, reducing the effect of the resonant scattering on heat conduction. The resonant scattering begins to diminish upon the onset of the spin transition of iron and eventually vanishes after the spin transition completes. This effect is due to the rearrangement of Fe^{2+} spin configuration, where the e_g energy levels become empty, while the t_{2g} levels are fully occupied by three paired electrons, eliminating the original energy degeneracy that gives rise to the Γ_{5g}–Γ_{4g}/Γ_{3g} transition and the resonant scattering. Evolution of the Fe^{2+} energy levels and spin configuration with pressure is illustrated in Fig. 1*B*. A survey of the literature shows that the onset pressure for the spin transition occurs at ~40–70 GPa at room temperature depending on the iron content, while the width of the spin transition is ~10–20 GPa (8). After the spin transition occurs, the thermal conductivity of Fp is expected to be further enhanced, because

the resonant scattering that suppresses the phonon transport begins to diminish. The bulk sound velocity V_Φ, however, softens during the spin transition (8, 13, 14) that would counterbalance the expected resonant scattering effect, since the thermal conductivity scales approximately with the square of sound velocity V, which includes longitudinal and transverse velocities (the faded region labeled HS + LS in Fig. 1*B* shows these two competing effects). The observed significant drop in the thermal conductivity of Fp56 at 53–62 GPa indicates that the softening effect of the bulk sound velocity is much more dominant than the resonant scattering effect. In Fp8 and Fp10, where the iron substitution becomes diluted, these two effects seem to have similar influences on the thermal conductivity, resulting in minimal changes in the conductivity across their respective spin transition. Due to these aforementioned effects, the thermal conductivity of iron-rich low-spin Fp is much lower than its iron-poor counterpart. That is, the compositional effect of iron substitution is expected to be more significant in the iron-rich low-spin Fp (Fig. 1).

Radial Profile of Lower-Mantle Thermal Conductivity. To build a radial model of lower-mantle thermal conductivity, we combined the thermal conductivity data for Fp measured in this study with recent data for Bm obtained with a similar method (29). In addition to pressure (depth) variations, thermal conductivity is affected by temperature and composition of the mantle aggregate: in our case, the proportion of Bm and Fp and the global iron content.

Based on our thermal conductivity data for Fp and literature data for pure MgO (25), and for Fe-Al-Bm (29), we parameterized the pressure dependence of the thermal conductivity. For each sample, we determined a best fit polynomial function of the conductivity as a function of pressure. Results are summarized in Table S2. Note that, in all cases except for $(Mg_{0.928}Fe_{0.072})SiO_3$, a linear fit describes the data well. Finally, to determine the radial profile of thermal conductivity as a function of depth, we simply used the pressure-to-depth function of preliminary reference Earth model (60).

Thermal conductivities of mantle materials are expected to decrease with increasing temperature following

$$\Lambda(T) \propto \frac{K}{T^n}, \qquad \textbf{[S1]}$$

where K is a parameter depending on the material, including its content in iron (see below), but not on temperature, and $0.5 \leq n \leq 1.0$ (25, 32, 33). For Fe-bearing minerals, n is typically assumed to be 0.5 (25, 32, 33), and we adopted this value in all of our calculations. For radial profiles of the thermal conductivity, we first fixed a potential (i.e., at zero pressure) temperature, T_p, and then added an adiabatic correction to account for the temperature increase due to pressure increase with depth, z. For simplicity, we assumed that the adiabatic gradient α is constant with z; that is,

$$T(z) = T_p + \alpha z. \qquad \textbf{[S2]}$$

In all calculations, we fixed α to 0.3 K km^{-1}, which is a reasonable value for the Earth's mantle and leads to an adiabatic increase in temperature of about 870 K at the CMB (z = 2,891 km).

Compositional changes in thermal conductivity include two sources: variations in mineralogical composition of the aggregate (here, Bm and Fp) and variations in iron fraction of each mineral composing the aggregate. To estimate the conductivity of lower-mantle aggregate at a given depth, we proceeded in two steps. First, we used our data and recent measurements for Bm (29) to calculate the conductivity of each mineral at given pressure and iron content. Second, we performed a relevant averaging of the conductivities of individual minerals. Variations due to mineralogical composition are controlled by fixing the volume fraction of Bm, X_{Bm}, in the aggregate. These experimental results allow quantification of the influence of iron on the conductivities of Bm and Fp by prescribing the fractions of iron in each of these minerals (x_{Fe}^{Bm} and x_{Fe}^{Fp}, respectively). Practically, variations of iron in the Earth's mantle are usually parameterized in terms of the global volume fraction of iron oxide, X_{Fe}, defined as

$$X_{Fe} = X_{Bm} x_{Fe}^{Bm} + (1 - X_{Bm}) x_{Fe}^{Fp}. \qquad \textbf{[S3]}$$

For given values of X_{Fe} and X_{Bm}, iron fractions of Bm and Fp can be obtained by prescribing the iron partitioning between Bm and Fp,

$$K_D = \frac{x_{Fe}^{Bm} / \left(1 - x_{Fe}^{Bm}\right)}{x_{Fe}^{Fp} / \left(1 - x_{Fe}^{Fp}\right)}, \qquad \textbf{[S4]}$$

and by solving simultaneously Eqs. **S3** and **S4**. Fig. S4 plots x_{Fe}^{Bm} and x_{Fe}^{Fp} as a function of K_D for X_{Bm} = 0.8 and several values of X_{Fe}. In the lowermost mantle ($z \geq$ 2,500 km), the global fraction of iron may vary by a few percent (3), typically between about 8 and 12%, and reasonable values of the iron partitioning are in the range of 0.2–0.4 (9, 12). This leads to values of x_{Fe}^{Bm} between 5 and 10% and values of x_{Fe}^{Fp} between 15 and 30%. Assuming that the rest of the mantle is mostly pyrolitic, with X_{Fe} = 9%, and for iron partitioning in the range of 0.2–0.4 (9, 12), x_{Fe}^{Bm} should be between 5 and 7%, and x_{Fe}^{Fp} should be between 16 and 22%. At the top of the lower mantle ($z \leq$ 1,200 km), iron partitioning may be substantially higher (12), around 0.6–0.8, leading to a more balanced partitioning of iron between Bm and Fp, with values of x_{Fe}^{Bm} between 8 and 9% and values of x_{Fe}^{Fp} between 10 and 12%.

To calculate the thermal conductivities of Bm and Fp at a fixed depth and for given iron fractions x_{Fe}^{Bm} and x_{Fe}^{Fp}, we performed simple linear interpolations using the parameterizations listed in Table S2. For Bm, a potential difficulty is that our previous measurements were available only up to x_{Fe}^{Bm} = 7.2% for Fe-bearing Bm and x_{Fe}^{Bm} = 12.9% for Fe-Al-Bm (29). Cases with x_{Fe}^{Bm} larger than 13% would, therefore, require extrapolating data from ref. 29, which may slightly bias the result, in particular if a saturation effect occurs at values of x_{Fe}^{Bm} larger than 13%. However, for K_D and X_{Fe} representative of the lower mantle, x_{Fe}^{Bm} never exceeds 10% (see above). In addition, for consistency, we only used data for Fe-Al-Bm to estimate lower-mantle thermal conductivity. This choice is further supported by the fact that Al-bearing Bm is present in mantle aggregate and may influence the iron partitioning. For Fp, one may point out that the data for pure MgO are available only up to a pressure of 60 GPa. Estimating thermal conductivity of pure MgO at larger pressure, therefore, requires extrapolating literature data, which may, again, bias the estimate of Fp thermal conductivity for cases with x_{Fe}^{Fp} smaller than 8%. Again, this case never occurs in practice, since for values of K_D and X_{Fe} relevant to the Earth mantle, x_{Fe}^{Fp} never falls below 10% (see above). One may point out that iron saturation effects in Fp may occur at values of x_{Fe}^{Fp} between those of our experimental samples (i.e., 10 and 56%). For saturation threshold larger than 25%, saturation effects would have no consequence on mantle conductivity, since for values of K_D and X_{Fe} representative of the lower mantle, x_{Fe}^{Fp} never exceeds 25% (Fig. S4). On the contrary, if saturation occurs for values of x_{Fe}^{Fp} between 10 and 25%, it may alter estimates of the thermal conductivity of Fp at lower-mantle condition. However, because Fp is present by only ~20% in mantle aggregate, the decrease in Fp conductivity due to the saturation effect would only slightly alter the estimated mantle conductivity. For instance, assuming a saturation threshold at x_{Fe}^{Fp} = 10% and taking K_D = 0.4, X_{Fe} = 9%, and T = 3,360 K, mantle conductivity

is equal to 7.74 W m^{-1} K^{-1} (i.e., only 5% smaller than the value estimated without accounting for saturation). Overall, our modeling approach for thermal conductivity of regular mantle and LLSVPs may not be affected by saturation effects. For stronger enrichments in iron, with X_{Fe} around 20% and higher, x_{Fe}^{Bm} and x_{Fe}^{Fp} are much larger. Linear extrapolation may then bias estimated conductivities, and saturation effects, although not constrained, should be taken into account (discussions on ULVZs) (Fig. 5).

A difficulty in estimating properties of a multiphase system is the choice of an appropriate averaging scheme. Different schemes, or estimators, may lead to very different estimates of aggregate properties, in particular if the properties of individual minerals differ by an order of magnitude or more (which is not the case here). The aggregate properties further depend on the grain distribution within the aggregate. Variational principles, however, allow definition of the narrowest possible bounds for a multiphase system, namely the Hashin–Shtrikman bounds (61). Here, we estimated the lower-mantle thermal conductivity at a given depth from the geometric average of Hashin–Shtrikman lower and upper bounds, Λ_{HS-} and Λ_{HS+}, respectively:

$$\Lambda_{<H\text{-}S>} = \sqrt{\Lambda_{HS-}\Lambda_{HS+}}. \quad \textbf{[S5]}$$

For a two-phase system composed of Bm and Fp and noting that Fp is more thermally conductive than Bm, the Hashin–Shtrikman lower and upper bounds in thermal conductivity are given as a function of the conductivities of Bm and Fp, Λ_{Bm} and Λ_{Fp}, and of the fraction of Bm, X_{Bm}, by

$$\Lambda_{HS-} = \Lambda_{Bm}\left[1 + \frac{(1-X_{Bm})(\Lambda_{Fp}-\Lambda_{Bm})}{\Lambda_{Bm} + X_{Bm}(\Lambda_{Fp}-\Lambda_{Bm})/3}\right] \quad \textbf{[S6]}$$

and

$$\Lambda_{HS+} = \Lambda_{Fp}\left[1 - \frac{X_{Bm}(\Lambda_{Fp}-\Lambda_{Bm})}{\Lambda_{Fp} - (1-X_{Bm})(\Lambda_{Fp}-\Lambda_{Bm})/3}\right]. \quad \textbf{[S7]}$$

In our case and after thermal and compositional corrections, the individual conductivity of Bm and Fp differs by about 20% at the top of the lower mantle and up to a factor of two at its bottom. This leads to rather narrow Hashin–Shtrikman bounds, with a typical width around 0.01 and 0.1 W m^{-1} K^{-1} at the top and bottom of the mantle, respectively (i.e., about 0.2 and 1.1% of the geometric average of Hashin–Shtrikman bounds, respectively). As an example, Table S3 lists Hashin–Shtrikman bounds and geometric average in thermal conductivity for the case T_p = 2,000 K, X_{Bm} = 0.8, and X_{Fe} = 0.09. We further calculated aggregate thermal conductivity from the Voigt–Reuss–Hill average, which is the mean of the arithmetic and harmonic averages and is often used to derive the thermoelastic properties of multiphase aggregates, but we found that this estimate predicts values of thermal conductivity slightly smaller than the lower Hashin–Shtrikman bound (Table S3) and should, therefore, be avoided.

Figs. S5 and S6 quantify the influences of spin transition in Fp and of depth variations of iron partitioning on thermal conductivity, respectively. In Fig. S5, dashed curves are calculated by removing the discontinuity due to the spin transition in ($Mg_{0.44}$, $Fe_{0.56}$)O data, while plain curves include it. In Fig. S6, dashed curves are obtained by fixing K_D to 0.25 throughout the lower mantle, whereas solid curves assume that K_D follows the radial model of Irifune et al. (12). Clearly, the effects of spin transition and iron partitioning on thermal conductivity are minor compared with those of temperature and composition. Accounting for spin transition decreases thermal conductivity by ∼0.05 W m^{-1} K^{-1} (i.e., only about 0.6% of the estimated aggregate conductivity). In the lowermost mantle, where the effects of changing iron partitioning are the most pronounced, the difference in thermal conductivity is about 0.2 W m^{-1} K^{-1}, ∼2.5% of the aggregate conductivity. By contrast, changing the temperature by 500 K, the iron content by 4%, or the fraction of Bm by 10% induces a change in thermal conductivity of about 1 W m^{-1} K^{-1} (Figs. 3 and 4) (i.e., ∼12% of the aggregate thermal conductivity).

Fig. 5 shows thermal conductivity for iron-rich, hot materials at the bottom of the mantle, which may provide an explanation for ULVZs observed locally at the bottom of the mantle (4, 5). In these calculations, the global iron fraction, X_{Fe}, is varied between 0.1 and 0.4, and the temperature is fixed to T = 3,760 K (Fig. 5*A*) and T = 4,160 K (Fig. 5*B*) (i.e., about 400 and 800 K higher, respectively, than the temperature along the T_p = 2,500 K adiabat; T = 3,360 K at 2,880 km). The fraction of Bm and iron partitioning are set to X_{Bm} = 0.9 and K_D = 0.4, respectively. We also accounted for possible iron saturation effects. Because there are, to date, no experimental constraints on the existence and threshold value of iron saturation, $x_{Fe(sat)}^{Bm}$, we tested several threshold values of $x_{Fe(sat)}^{Bm}$ in the range of 12.9–30%. Iron saturation in Fp is less sensitive, and thus, we only imposed saturation threshold at $x_{Fe(sat)}^{Fp}$ = 56%, corresponding to our experimental data with higher iron fraction. For comparison, the estimated thermal conductivity for average mantle (X_{Bm} = 0.8, X_{Fe} = 0.09, and T = 3,360 K) at a depth of z = 2,880 km is indicated with the thick horizontal dashed line in Fig. 5. Thermal conductivity strongly decreases with increasing iron fraction, whatever the iron partitioning K_D. It further decreases with increasing iron partitioning and increasing fraction of Bm. This latter observation is interesting, because ULVZs are preferentially found within or at the edges of LLSVPs (46), which are believed to be enriched in Bm by up to 10%, compared with the average mantle. Taking X_{Bm} = 0.9 and K_D = 0.4, the thermal conductivities predicted by the modeling of our data are then equal to ∼6.3 and ∼1.7 W m^{-1} K^{-1} for enrichments in iron of 3% (X_{Fe} = 12%) and 21% (X_{Fe} = 30%), respectively. These values are lower than the estimated thermal conductivity for the average mantle (blue curve in Fig. 3) by 23 and 80%, respectively. If iron saturation is accounted for, thermal conductivity for X_{Fe} = 30% remains lower than the reference conductivity for lower mantle by at least 30% [$x_{Fe(sat)}^{Bm}$ = 12.9%] and up to ∼80% [$x_{Fe(sat)}^{Bm}$ = 30%]. Note that, in this latter case, the threshold value is not reached, since for X_{Bm} = 0.9 and K_D = 0.4, the fraction of iron in Bm is x_{Fe}^{Bm} = 27.9%. If hot and strongly enriched in iron, ULVZs may, therefore, have a very low thermal conductivity compared with their surroundings, which in turn, may have delayed their cooling.

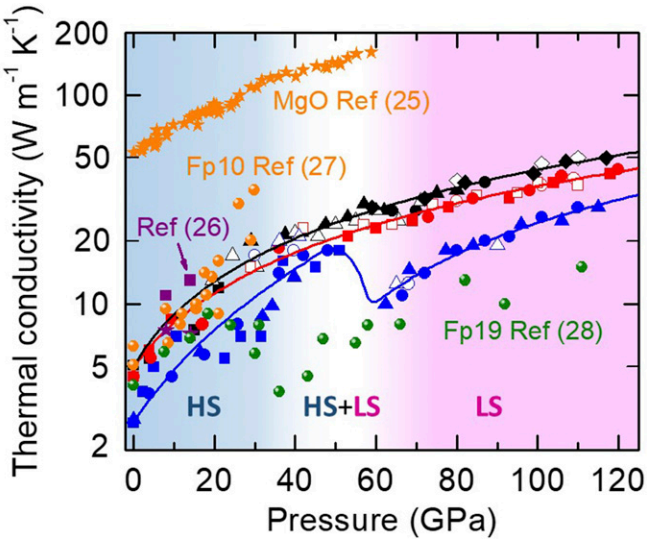

Fig. S1. Comparison of the lattice thermal conductivity of (Mg,Fe)O Fp at high pressures and room temperature. The thermal conductivities of (Mg,Fe)O are smaller than the MgO (orange stars) from ref. 25 due to the Fe substitution effect. Our data for the Fp10 (red symbols) are in good agreement with previous results in ref. 27 (orange circles) before 20 GPa, after which the literature data increase drastically with large uncertainty. Literature data for Fp19 (green circles) from ref. 28 and Fp5 (purple squares) and Fp20 (purple stars) at 370 K from ref. 26 are plotted for comparison. The Fp19 data begin to decrease with pressure around 20 GPa, much lower than the typical pressure range of spin transition (40–60 GPa), and become substantially smaller than our Fp10 and Fp56 as well as the previous Fp10 data (orange circles) after 20 GPa. The symbols for our results of (Mg,Fe)O with different iron contents are the same as in the text. As in Fig. 1, the blue and red shaded areas show the pressure ranges where Fe^{2+} ions are in the high-spin (HS) and low-spin (LS) states, respectively. The faded region in between indicates the spin transition zone (HS + LS).

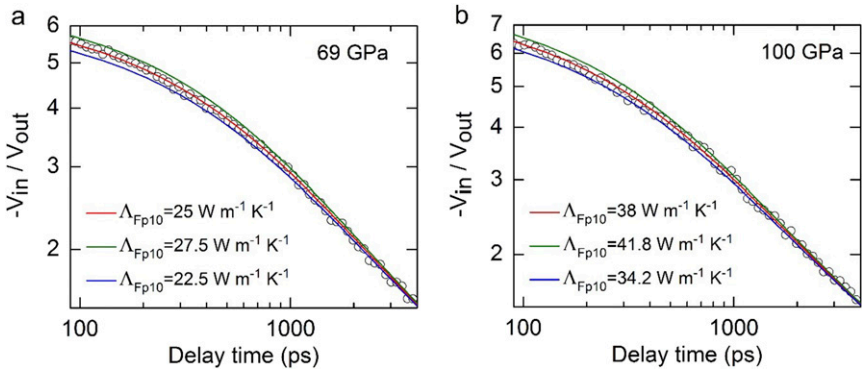

Fig. S2. Representative high-pressure TDTR spectra of Fp10 with calculations using a heat flow model. Experimental spectra for the ratio $-V_{in}/V_{out}$ as a function of delay time between pump and probe pulses are shown as circles. Solid curves represent calculations using a heat flow model with different values of Fp10 thermal conductivity Λ_{Fp10}. At 69 GPa (*A*) and 100 GPa (*B*), Λ_{Fp10} = 25 and 38 W m^{-1} K^{-1} (red curves), respectively, provide a best fit to the data using input parameters listed in Table S1. In our experimental conditions, the ratio $-V_{in}/V_{out}$ is sensitive to the Λ_{Fp10} during delay time of few hundred picoseconds, particularly from 100 to 500 ps (53, 59). A test of 10% change in Λ_{Fp10} (green and blue curves) results in a clear deviation from the best fit to the data, which shows that the heat flow model fitting and derived Λ_{Fp10} are precise and highly reliable because of our high-quality data and sample geometry.

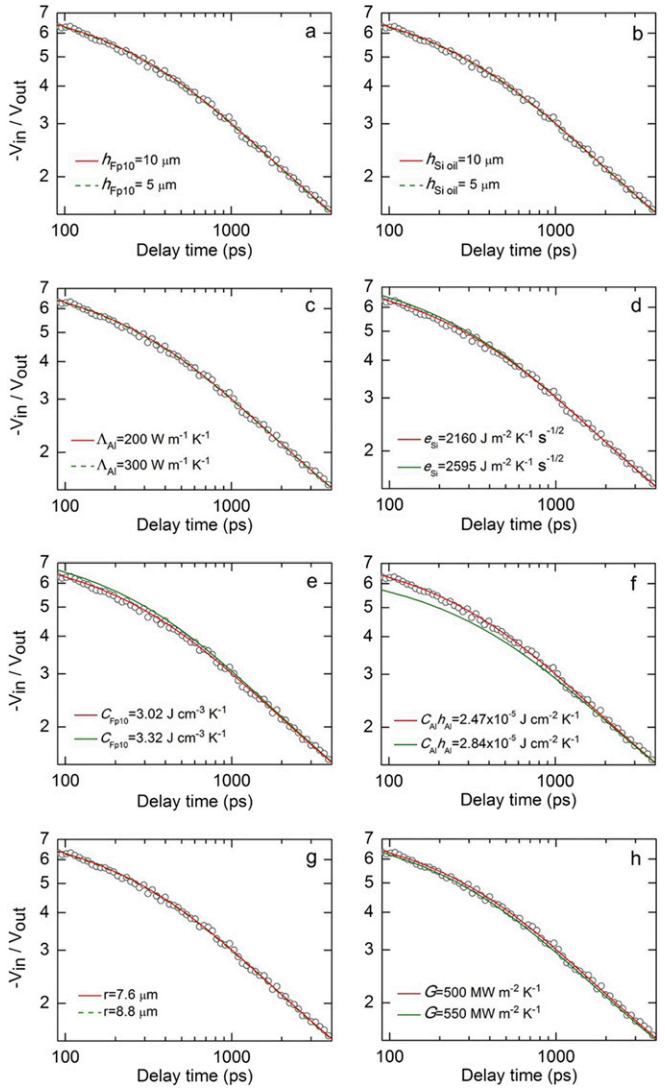

Fig. S3. Tests of sensitivity of the heat flow model to input parameters for Fp10 at 100 GPa. The Fp10 thermal conductivity Λ_{Fp10} is fixed to be 38 W m^{-1} K^{-1} using input parameters listed in Table S1. (*A* and *B*) Changes in the thicknesses of Fp10 (h_{Fp10}) and silicone oil ($h_{Si\ oil}$), respectively, by even 50% show identical fits to the data, indicating that uncertainties in their thicknesses have no effect on the Λ_{Fp10}. (*C*) Since the Al thermal conductivity, Λ_{Al}, is large, it has minimal influence on the Λ_{Fp10}. (*D*) An example change of 20% thermal effusivity of the pressure medium silicone oil, $e = (\Lambda_{Si}C_{Si})^{1/2}$, slightly deviates the model fit from the data, which requires a small decrease of Λ_{Fp10} from 38 to 37 W m^{-1} K^{-1} to refit the data (i.e., introducing approximately only 2.7% uncertainty to the Λ_{Fp10}). (*E*) An example 10% uncertainty in the volumetric heat capacity of Fp10, C_{Fp10} (3.02–3.32 J cm^{-3} K^{-1}), again deviates the model fit very slightly from the data, requiring Λ_{Fp10} to decrease slightly to 35 W m^{-1} K^{-1} to fit the data (i.e., ~8% uncertainty to the Λ_{Fp10}) (*F*) Influence of the Al heat capacity per unit area, the product of volumetric heat capacity and thickness, C_{Al} h_{Al}. [The ratio $-V_{in}/V_{out}$ at a few hundred picoseconds delay time scales inversely with C_{Al} h_{Al} (53).] An example uncertainty of 15% requires 24% change in the Λ_{Fp10} to fit the data. (*G*) Laser spot size changed by 15% (7.6–8.8 μm) has essentially no effect on the Λ_{Fp10}. (*H*) Thermal conductance of Al/Fp10 interface and Al/silicone oil interface, *G*, has minor effect on the Λ_{Fp10}. Variations in the interface thermal conductance change the slope of model fitting curve at longer delay time, typically longer than 1,000 ps (53, 59). A 10% uncertainty has already made the model fitting curve unable to fit the data well after 1,000 ps. The uncertainty in the interface thermal conductance, therefore, is typically less than 10%, which only propagates 4% uncertainty in the derived Λ_{Fp10}.

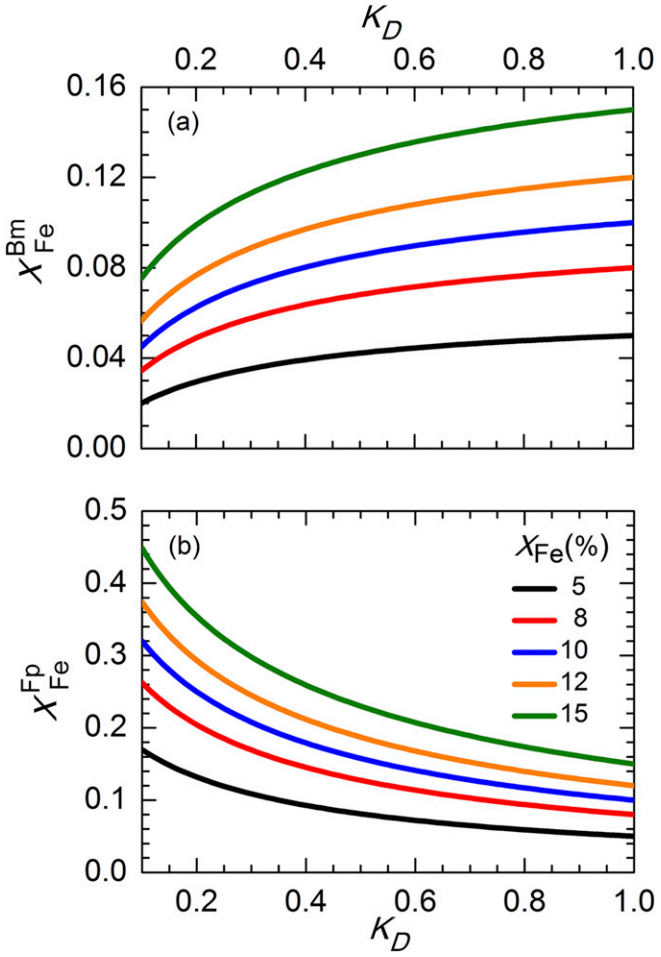

Fig. S4. Fractions of iron in (*A*) Bm, x^{Bm}_{Fe}, and (*B*) Fp, x^{Fp}_{Fe}, obtained by solving Eqs. **S3** and **S4**. Results are shown as a function of the iron partitioning K_D and for several values of the global iron fraction, X_{Fe} (color code). The fraction of Bm is set to $X_{Bm} = 0.8$.

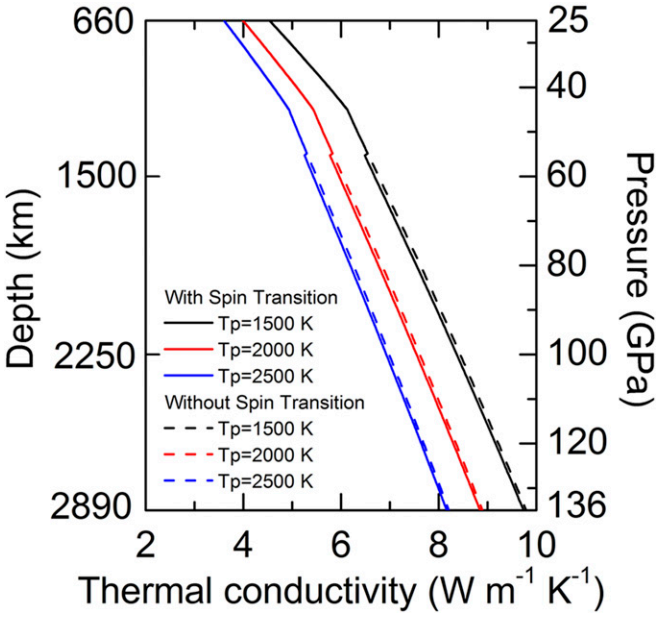

Fig. S5. Lattice thermal conductivity profile for the lower mantle with and without the effect of spin transition in Fp. The spin transition has minimal influence on the lower-mantle thermal conductivity. The fraction of Bm and the global iron fraction are set to $X_{Bm} = 0.8$ and $X_{Fe} = 0.09$, respectively, and iron partitioning K_D is changed with depth based on the results of Irifune et al. (12). Data for Bm are from Fe-Al-Bm (29).

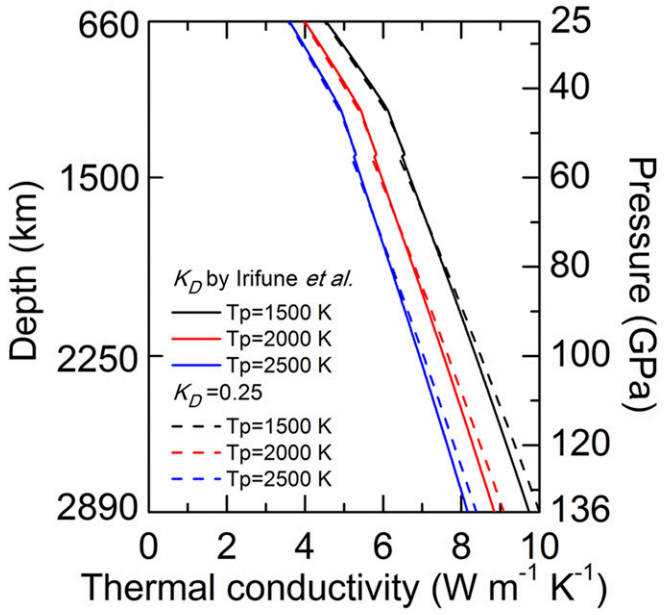

Fig. S6. Comparison of the lattice thermal conductivity profile for the lower mantle, with iron partitioning K_D changing with depth taken from Irifune et al. (12) and K_D being a constant of 0.25. The K_D has a small influence on the lower-mantle thermal conductivity. The fraction of Bm and the global iron fraction are set to X_{Bm} = 0.8 and X_{Fe} = 0.09, respectively. Data for Bm are from Fe-Al-Bm (29). For Fp, the effect of spin transition is included.

Table S1. Input parameters for the bidirectional heat flow model at two representative pressures of 69 and 100 GPa

P, GPa	C_{Fp10}, J cm^{-3} K^{-1}	C_{Al}, J cm^{-3} K^{-1}	h_{Al}, nm*	$e = (\Lambda_{Si}C_{Si})^{1/2}$, J m^{-2} K^{-1} s$^{-1/2}$	r, μm	$h_{Fp10/Si\ oil}$, μm	Λ_{Al}, W m^{-1} K^{-1}	G, MW m^{-2} K^{-1}
69	3.21	2.68	94.0	1,954	7.6	10	200	380
100	3.02	2.69	92.1	2,160	7.6	10	200	500

C_{Al}, Al heat capacity; C_{Fp10}, Fp10 heat capacity; e, silicone oil thermal effusivity; G, thermal conductance of Al/Fp10 and Al/silicone oil interfaces; h_{Al}, Al thickness; $h_{Fp10/Si\ oil}$, Fp10 thickness/silicone oil thickness; Λ_{Al}, Al thermal conductivity; r, laser spot size.
*In this experimental run, the Al thickness at ambient pressure is 110.7 nm.

Table S2. Pressure dependence of thermal conductivity

Mineral	Pressure, GPa	a_0, W m^{-1} K^{-1}	a_1, W m^{-1} K^{-1} GPa^{-1}	a_2, W m^{-1} K^{-1} GPa^{-2}	Source
$MgSiO_3$	0–120	5.873	0.181		Ref. 29
$(Mg_{0.928},Fe_{0.072})SiO_3$	0–45	4.689	0.054	4.41×10^{-3}	Ref. 29
$(Mg_{0.928},Fe_{0.072})SiO_3$	45–120	20.032	−0.202		
$(Mg_{0.886},Fe_{0.129})(Al_{0.115}Si_{0.906})O_3$	0–45	5.217	0.206		Ref. 29
$(Mg_{0.886},Fe_{0.129})(Al_{0.115}Si_{0.906})O_3$	45–120	12.597	0.042		
MgO	0–60	50.645	1.878		Ref. 25
$(Mg_{0.92},Fe_{0.08})O$	0–120	5.033	0.388		This study
$(Mg_{0.90},Fe_{0.10})O$	0–120	4.959	0.316		This study
$(Mg_{0.44},Fe_{0.56})O$	0–55	2.732	0.310		This study
$(Mg_{0.44},Fe_{0.56})O$	55–120	−11.189	0.356		

For each sample measured in this study and from refs. 25 and 29, we parameterized the thermal conductivity as a function of pressure P following $\Lambda(P) = a_0 + a_1P + a_2P^2$.

Table S3. Thermal conductivities at different depths for the case $T_p = 2{,}000$ K, $X_{Bm} = 0.8$, and $X_{Fe} = 0.09$ using the parameterizations for Fp and Fe-Al-Bm in Table S2

Depth, km	Pressure, GPa	Λ_{Bm}, W m^{-1} K^{-1}	Λ_{Fp}, W m^{-1} K^{-1}	Λ_{HS-}, W m^{-1} K^{-1}	Λ_{HS+}, W m^{-1} K^{-1}	$\Lambda_{<H\text{-}S>}$, W m^{-1} K^{-1}	Λ_{VRH}, W m^{-1} K^{-1}
1,000	38.54	4.716	6.189	4.988	4.992	4.990	4.981
1,500	62.00	5.600	8.042	6.038	6.048	6.043	6.025
2,000	86.96	6.326	10.436	7.026	7.059	7.043	7.007
2,500	113.52	7.059	12.967	8.025	8.092	8.059	8.004
2,800	130.23	7.508	14.506	8.629	8.722	8.675	8.609

Λ_{Bm} and Λ_{Fp} are the conductivities of Bm and Fp, respectively. Λ_{HS-} and Λ_{HS+} are the Hashin–Shtrikman lower and upper bounds, respectively. $\Lambda_{<H\text{-}S>}$ is the geometric average of these bounds, and Λ_{VRH} is the Voigt–Reuss–Hill average.